Inferring Transmission Dynamics of Respiratory Syncytial Virus from Houston Wastewater

Jose R. Palacio^{*1}, Katherine B. Ensor¹, Sallie A. Keller², Rebecca Schneider³, Kaavya Domakonda³, Loren Hopkins^{1,3}, and Lauren B. Stadler⁴

¹Department of Statistics, Rice University, 6100 Main St, Houston, TX, USA

²Biocomplexity Institute, University of Virginia, Charlottesville, VA, USA

 ³Houston Health Department, Houston, TX, USA
⁴Department of Civil and Environmental Engineering, Rice University, Houston, TX, USA

November 25, 2025

Abstract

Wastewater-based epidemiology (WBE) is an effective tool for tracking community circulation of respiratory viruses. We address estimating the effective reproduction number (R_t) and the relative number of infections from wastewater viral load. Using weekly Houston data on respiratory syncytial virus (RSV), we implement a parsimonious Bayesian renewal model that links latent infections to measured viral load through biologically motivated generation and shedding kernels. The framework yields estimates of R_t and relative infections, enabling a coherent interpretation of transmission timing and phase. We compare two input strategies—(i) raw viral-load measurements with a log-scale standard deviation, and (ii) state-space-filtered load estimates with time-varying variances—and find no practically meaningful differences in inferred trajectories or peak timing. Given this equivalence, we report the filtered input as a pragmatic default because it embeds week-specific variances while leaving epidemiological conclusions unchanged.

Keywords

Respiratory Syncytial Virus (RSV), Wastewater-based Epidemiology, Renewal Model, Effective Reproduction Number (R_t) , Bayesian Inference

^{*}Corresponding author: jrp16@rice.edu

1 Introduction

Wastewater-based epidemiology (WBE) has established itself as a crucial tool for population-level surveillance of infectious diseases. By quantifying viral genetic material in wastewater, WBE provides a non-invasive and cost-effective monitoring system that can capture early signals of community transmission, independent of medical care-seeking or clinical testing capacity. However, translating these signals into absolute infection counts is challenging due to substantial variability in viral shedding, biological and physical delays in the sewer network, and measurement uncertainty. In practice, it is therefore more informative and robust to focus on relative transmission metrics—most notably the effective reproduction number (R_t) , which captures temporal changes in transmission dynamics (Huisman et al., 2022; Champredon et al., 2024).

To date, much of the literature has centered on SARS-CoV-2, for which wastewater data have demonstrably supported the public health response. Extending WBE to other pathogens poses additional challenges. For respiratory syncytial virus (RSV)—a leading cause of severe respiratory illness in infants, older adults, and immunocompromised individuals (Mayo Clinic Staff, 2023)—clinical surveillance is affected by underreporting and reporting delays. Many RSV cases are managed at home without hospitalization, so clinical records may not fully reflect community circulation. In wastewater, signal interpretation is further complicated by heterogeneity across treatment plants and the populations they serve (Haak et al., 2022), as well as by incubation, shedding dynamics, and transport processes in the sewer system (He et al., 2020; Hart and Halden, 2020).

Despite these challenges, RSV is consistently detectable in wastewater, and recent studies highlight its potential as a complement to clinical surveillance (Hughes et al., 2021). Large-scale, systematic analyses in dense urban networks remain scarce, however, leaving open questions about the robustness, comparability, and epidemiological value of wastewater signals (Wade et al., 2022).

Multi-stage models are common in environmental epidemiology. In a typical two-stage setup, stage one fits separate models for each unit (e.g., locations or studies) to produce unit-level summaries of the association of interest; stage two then aggregates those summaries to obtain an overall estimate (Sera and Gasparrini, 2022). Related Bayesian approaches follow the same spirit: analyze each unit independently, then pass those unit-level posteriors or estimates into a second-stage model that treats them as draws from a common population, allowing for uncertainty propagation (Lunn et al., 2013).

In this vein, we adopt a two-stage strategy: outputs from a hierarchical state-space model serve as inputs to a Bayesian model, and we use the resulting posterior to derive downstream epidemiological metrics. The emphasis is on the workflow—separating estimation tasks into modules and carrying forward uncertainty—rather than on any specific implementation detail from prior papers.

Here we outline the structure of the manuscript. Section 2 (Methodology) details the data, the renewal model with generation and shedding kernels, the latent dynamics of R_t and I_t , the estimation procedure in nimble (de Valpine et al., 2024), and the modular integration with the Kalman filter (SSM). Section 3 (Results) presents convergence diagnostics and parameter estimates, and compares R_t and I_t trajectories across three input/noise specifications (A–C), with an emphasis on the 69th Street plant and sensitivity analyses. Section 4 (Discussion) interprets the key findings—including practical invariance to input choice and stability across unit changes—and their implications for

2 Statistical Framework and Methodology

In this work, we analyze weekly RSV viral load expressed in billions of genome copies per day (B gc/day) for a single wastewater treatment plant, the 69th Street WWTP in Houston. Loads are constructed by multiplying observed concentrations (gc/L) by the plant's median daily influent flow (L/day) and rescaling by 10^9 :

$$y_t = C_t F \times 10^{-9}, \qquad t = 1, \dots, T,$$

where C_t is the RSV concentration in week t (gc/L), and F is the median daily influent flow for the wastewater treatment plant (L/day). The resulting y_t denotes viral load in B gc/day. The City of Houston operates 38 facilities serving populations from > 600 to > 500,000 residents (Houston Public Works, 2023); serving 2.2 million residents. Twentyfour-hour composite samples were collected weekly each Monday between January 16, 2023, and December 30, 2024; values below the laboratory limit of detection (LOD) are treated as missing.

We focus on the 69th Street WWTP, the largest facility in Houston, which serves an estimated 551,150 residents. Its size, broad catchment area, and consistent sampling make it one of the city's most reliable wastewater signals. By concentrating on this plant, we reduce cross-plant heterogeneity and create a clearer setting to test and refine our modeling framework, establishing a methodological benchmark for future extensions across Houston's network.

We adopt a Bayesian renewal-based framework widely used in wastewater epidemiology (Fraser, 2007; Huisman et al., 2022; Champredon et al., 2024). These models link latent infections to wastewater viral loads through two key temporal processes: the generation interval, which governs the renewal of infections, and the shedding profile, which maps past infections to the viral RNA signal.

Whereas pipelines such as EpiSewer adopt a modular structure to incorporate incubation, shedding, and generation dynamics in detail (Lison et al., 2023), our version is deliberately less complex. This simplification facilitates interpretation of both the latent transmission process and the plant-specific scaling parameters, while retaining the ability to capture epidemic dynamics from wastewater signals.

We complement the renewal framework with information from a state-space model estimated via the MARSS package (Holmes et al., 2012). These filtered signals are propagated into the renewal model, allowing us to evaluate robustness and provide an additional perspective on how to evaluate infection dynamics.

Transmission and observation delays are represented by two kernels: the generation interval and the shedding profile. Both are modeled as Gamma distributions in continuous time and discretized into weekly lags using cumulative distribution function differences. This construction is standard in renewal-based epidemic models (Fraser, 2007; Huisman et al., 2022; Champredon et al., 2024).

The generation interval governs the renewal of infections. Following (Vink et al., 2014), we assume a mean of 7.5 days and a standard deviation of 2.1 days for RSV infections. These values are expressed through a Gamma distribution whose parameters are derived from the reported mean and variance. To obtain weekly weights, we discretize the continuous distribution into intervals centered at integer lags. The support is truncated

at G weeks, where G denotes the maximum lag retained in the kernel. Probability mass beyond G is not used, and the retained weights are renormalized to sum to one, following a similar construction to that in (Bracher and Held, 2022).

For the generation interval, support is therefore $g=1,\ldots,G$, excluding lag zero to reflect the biological delay between primary and secondary infections (Fraser, 2007; Huisman et al., 2022):

$$w_q^{\text{gen}} \propto F_{\Gamma} \left(g + \frac{1}{2}; \, \kappa_{\text{GI}}, \theta_{\text{GI}} \right) - F_{\Gamma} \left(g - \frac{1}{2}; \, \kappa_{\text{GI}}, \theta_{\text{GI}} \right).$$
 (1)

The shedding profile maps latent infections to RNA viral loads in wastewater. Based on clinical evidence synthesized by (Cevik et al., 2023), we assume a mean of 4.6 days and a standard deviation of 2.0 days for the duration of viral shedding. These values are expressed through a Gamma distribution whose parameters are derived from the reported mean and variance. Because our data are aggregated weekly, the interpretation of lag zero differs from daily formulations: here, d=0 corresponds to contributions occurring within the same calendar week as infection, which is biologically plausible given that RSV shedding can begin within the first few days of illness (Hall et al., 2001; DeVincenzo et al., 2005).

As in (1), we use a finite support d = 0, ..., D; the mass beyond D is omitted and the remaining weights are renormalized to sum to one.

$$w_d^{\text{shed}} \propto F_{\Gamma} \left(d + \frac{1}{2}; \, \kappa_{\text{SH}}, \theta_{\text{SH}} \right) - F_{\Gamma} \left(\max\{d - \frac{1}{2}, \, 0\}; \, \kappa_{\text{SH}}, \theta_{\text{SH}} \right).$$
 (2)

2.1 Latent Transmission Process

The effective reproduction number R_t is modeled through a scaled softplus transformation of an unconstrained latent link—scale process z_t (a unitless transmission-intensity index) (Scott et al., 2021; Lison et al., 2023). This transformation guarantees positivity of R_t and behaves approximately like the identity in the epidemiologically relevant neighborhood of $R_t \approx 1$, while remaining numerically stable:

$$R_t = \frac{\log(1 + \exp(kz_t))}{k}, \qquad k > 0.$$

The parameter k controls the curvature of the link between z_t and R_t . Larger values yield a sharper response (approaching a rectified-linear mapping for positive z_t), amplifying short-lived increases in transmission, whereas smaller values produce a smoother, more graded mapping. Thus, k regulates how strongly fluctuations in the latent process translate into changes in transmissibility.

The latent process $\{z_t\}$ evolves according to a Gaussian random walk, providing a parsimonious yet flexible representation of temporal changes in transmission:

$$z_1 \sim \mathcal{N}(1, \sigma_{\epsilon}^2), \qquad z_t \sim \mathcal{N}(z_{t-1}, \sigma_{\epsilon}^2), \quad t \ge 2,$$

with $\sigma_{\epsilon} > 0$ controlling week-to-week volatility.

Let I_t denote the number of new infections during week t. Following the renewal formulation (Fraser, 2007), expected incidence is expressed as a convolution of past infections with the generation-interval distribution:

$$\lambda_t = R_t \sum_{g=1}^G w_g^{\text{gen}} I_{t-g}, \text{ where } I_t \sim \text{Poisson}(\lambda_t), \quad t \ge 2,$$

and w_g^{gen} are the generation-interval weights normalized to sum to one and G is their maximum support.

Because absolute infections cannot be identified from wastewater alone, the magnitude of I_t depends on the initial condition, which we set to the citywide average weekly RSV healthcare encounter data multiplied by the share of the city's population in the service area (Houston Health Department, 2025).

2.2 Viral Load Process

We link latent infections to RNA viral loads through the shedding kernel $\{w_d^{\text{shed}}\}_{d=0}^D$, which encodes the timing of viral release after infection. Using (2), the expected load is

$$\pi_t = \beta \sum_{d=0}^{D} I_{t-d} \, w_d^{\text{shed}},$$

where $\beta > 0$ converts infections into billions of genome copies per day per infection.

The viral loads are modeled by a log-normal likelihood:

$$\mu_t = \log(\pi_t) - \frac{1}{2}\sigma_y^2, \quad y_t \sim \text{LogNormal}(\mu_t, \sigma_y^2),$$

where $\sigma_y > 0$ captures measurement variability on the log scale. This parametrization implies $\mathbb{E}[y_t \mid \pi_t] = \pi_t$ and is standard in wastewater applications with multiplicative experimental and sampling variability.

2.3 State-space model

We also obtain filtered trajectories from a non-linear Gaussian state—space model (SSM) and propagate their time-varying variances as known observation uncertainty. This alternative input is used to check whether inferences are sensitive to prefiltering, while allowing week-specific variances to be carried into the renewal likelihood.

Our methodologies account for noise and missing data in the wastewater time series while separating persistent structure from high-frequency variability. We implement this step with the MARSS package in R (Holmes et al., 2012).

Following the approach in (Ensor et al., 2025), let x_t denote the latent wastewater RNA viral load on a log-scale at time t with initial state $x_0 \sim \mathcal{N}(\psi, 1)$ where ψ is unknown. The state equation is the first difference twice or

$$x_t = 2x_{t-1} - x_{t-2} + w_t, \quad w_t \sim \mathcal{N}(0, \sigma_w^2),$$

where w_t is a Gaussian innovation with mean zero and variance σ_w^2 .

The observation equation is given by

$$y_t = x_t + v_t, \quad v_t \sim \mathcal{N}(0, \sigma_v^2),$$

where y_t denotes the measured viral load on a log scale in week t, and v_t represents measurement error; assumed Gaussian with mean zero and variance σ_v^2 .

The parameters of the SSM namely σ_v , σ_w , and ψ via maximum likelihood, yielding filtered estimates of the latent trend and its pointwise uncertainty:

$$\widehat{x}_{t|t} = E[x_t|y_{1:t}], \quad \widehat{P}_{t|t} = Var[x_t | y_{1:t}].$$

These variances are later used to construct uncertainty bands and to propagate measurement uncertainty into subsequent modeling layers. Importantly, estimation is performed on the log-10 scale and subsequently converted to the natural measurement scale (gc/L), ensuring consistency with the log-normal likelihood adopted in the measurement layer of the renewal model.

Finally, to assess robustness to measurement noise, we first fit the renewal model to the viral-load measurements y_t while injecting week-specific observation variances from the Kalman filter. We then replace y_t with the SSM filtered trajectories \hat{y}_t , again using \hat{P}_t as known variances. As shown in Section 3, the resulting trajectories are practically equivalent; accordingly, we present the SSM-filtered input as the default and treat the direct-measurement fit as a robustness check.

We estimated the parameters of the Bayesian renewal model in nimble via MCMC. The sampler jointly sampled the latent trajectories and the key parameters, producing posterior draws for all unknown quantities. We run multiple chains and discard the warm-up iterations. We assessed convergence using the rank-normalized split \hat{R} and verified well-mixed chains using the relative Monte Carlo standard error (relMCSE). Finally, for the state-space model, we performed the estimations using maximum likelihood with the BFGS as our optimization option in the MARSS package, which utilizes Kalman filtering for efficient likelihood evaluation.

In the Bayesian layer of the renewal model, the latent driver z_t follows a Gaussian random walk with a diffuse normal prior for z_1 and a log-normal prior on the innovation scale σ_{ϵ} . The softplus curvature parameter k is assigned a truncated log-normal prior to ensure positivity and a stable mapping between z_t and R_t . When β is estimated, we place a normal prior on $\log \beta$, inducing a log-normal prior on the natural scale. The observation standard deviation, σ_y , is either supplied externally as a time-varying sequence or treated as a single unknown parameter with a truncated normal prior. All priors are moderately informative, providing reasonable regularization while allowing the likelihood to dominate the inference. The mean of the initial state ψ in the state-space model is estimated separately via maximum likelihood.

3 Results

In this section, we present results from applying the Bayesian renewal model to RSV data from the WWTP under two specifications: (A) viral-load measurements transformed to billions of copies per day (BCPD) with a homoscedastic observation variance σ_y estimated; and (B) state-space—model (SSM) filtered trajectories \hat{y}_t used as the observation input, with week-specific variances \hat{P}_t treated as known.

Results are organized as follows:

- 1. Convergence diagnostics and parameter estimates, summarizing stability and consistency across fits; and
- 2. Latent trajectories of incidence (I_t) and effective reproduction number (R_t) , comparing the raw viral-load input versus the filtered input.

3.1 Diagnostics

Table 1 summarizes posterior estimates and convergence diagnostics for the scalar parameters under two specifications: (A) viral-load measurements as input with homoscedastic

noise (a single σ_y); and (B) SSM-filtered estimates of the viral load with heteroscedastic noise (\hat{P}_t). Convergence is strong in both cases: rank-normalized split \hat{R} values lie between 1.003 and 1.018, and relative Monte Carlo standard errors (relMCSE) are small ($\approx 0.002\text{--}0.023$), indicating well-mixed chains for all parameters. The link-curvature parameter k centers around 8 with $\hat{R} \leq 1.007$ (relMCSE ≤ 0.009), consistent with a moderately sharp softplus mapping from z_t to R_t . The innovation standard deviation σ_ϵ is small in both specifications (A: 0.073; B: 0.078), suggesting gradual week-to-week changes in transmission. In specification A, dispersion is summarized by $\hat{\sigma}_y \approx 0.385$ ($\hat{R} = 1.003$, relMCSE = 0.002), whereas in specification B the observation heteroscedasticity is encoded via the time-varying \hat{P}_t . Overall, posterior summaries are broadly similar across specifications: point estimates differ slightly, but credible intervals overlap and convergence metrics are comparable.

For the plant-specific scale, β is 13.827 (SD 3.646; 95% CI [7.838, 22.273]) in A and 14.737 (SD 3.969; 95% CI [8.591, 23.945]) in B; the credible intervals overlap, indicating no practical difference in scale across the two specifications. All parameters are well identified, and the diagnostics (\hat{R} and relMCSE) show comparable sampling performance in A–B. Conceptually, using filtered inputs with time-varying variances \hat{P}_t provides an alternative to the homoscedastic model without changing the qualitative conclusions about transmission dynamics.

	A					
	Mean	SD	95% CI	$\widehat{R}/\mathrm{relMCSE}$		
β	13.827	3.646	[7.838, 22.273]	1.008 / 0.020		
k	8.238	4.691	[2.122, 18.681]	$1.007 \ / \ 0.008$		
σ_ϵ	0.073	0.028	[0.030, 0.135]	$1.008 \ / \ 0.023$		
σ_y	0.385	0.038	[0.316,0.466]	$1.003\ /\ 0.002$		
	В					
	Mean	SD	95% CI	$\widehat{R}/\mathrm{relMCSE}$		
β	14.737	3.969	[8.591, 23.945]	1.018 / 0.021		
k	8.026	4.727	[1.765, 18.600]	$1.005 \ / \ 0.009$		
σ_ϵ	0.078	0.027	[0.032, 0.137]	1.017 / 0.019		
σ_y			_			

Table 1: Posterior means, standard deviations, 95% credible intervals, and convergence diagnostics ($\hat{R}/\text{relMCSE}$) for scalar parameters under two specifications: (A) BCPD with homoscedastic σ_y estimated; (B) SSM-filtered viral-load inputs with week-specific variances \hat{P}_t treated as known.

3.2 Latent infections and transmission dynamics from wastewater

Figure 1 displays posterior means and 95% credible bands for latent incidence (I_t) overlaid with wastewater viral load. Across both specifications (A–B), I_t rises sharply in late 2023, drops in January 2024, remains low through mid-2024, and shows a moderate uptick in

autumn 2024. Timing is coherent: the I_t peak precedes the load maximum by roughly one week in each case. Phase, peak timing, and overall I_t trajectories are practically indistinguishable across inputs. Because the absolute scale of I_t is not identified from wastewater alone, we interpret I_t in relative terms and anchor its level via the initial condition.

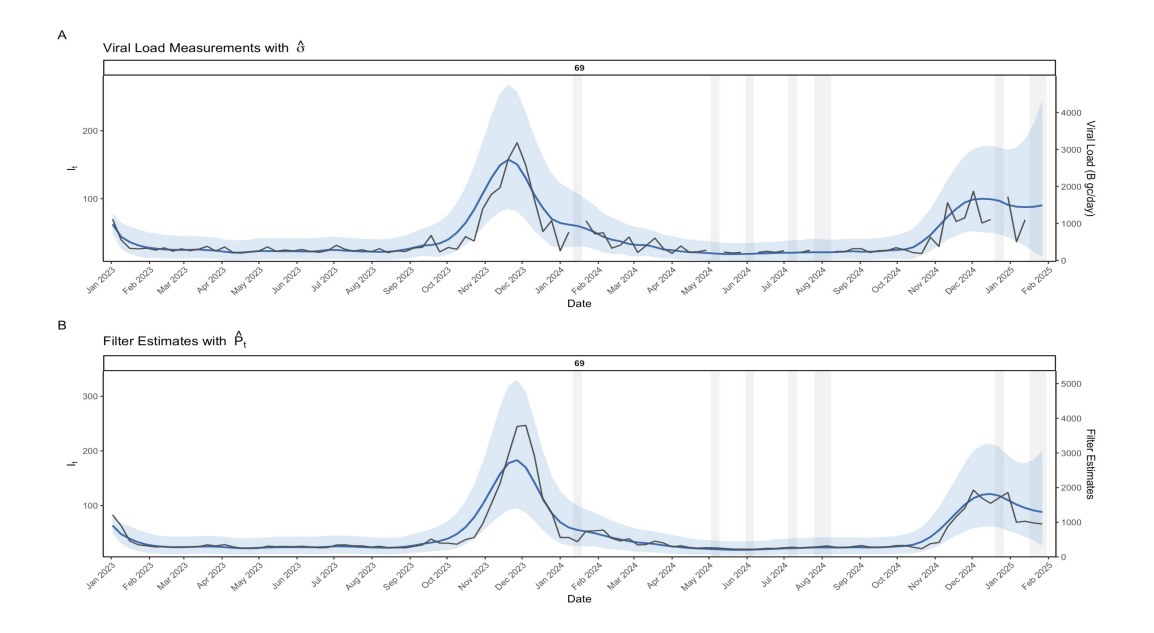


Figure 1: Latent incidence (I_t) with viral load on the right axis. Blue line: posterior mean of I_t ; blue band: 95% credible interval; gray line: viral load (B gc/day). Panels A–B correspond, respectively, to: (A) BCPD with homoscedastic observation variance σ_y estimated; and (B) SSM-filtered trajectories with week-specific variances \hat{P}_t treated as known. Gray vertical bands represent periods with missing wastewater measurements.

Figure 2 reports the effective reproduction number (R_t) . Across both specifications (A–B), R_t is subcritical (< 1) in early 2023, becomes clearly supercritical in autumn 2023, and drops below 1 around December–January; a smaller episode appears in autumn 2024. For 69th Street (October 2023–February 2024), the peaks occur on October 23 and 30 for R_t , November 20 and 27 for I_t , and November 27 and December 4 for the load (top and bottom panels, respectively). In both specifications, the R_t maximum leads the load maximum by about five weeks. The ordering $R_t \rightarrow I_t \rightarrow$ load holds and is consistent with the generation and shedding kernels (about 1–2 weeks) and weekly aggregation. The inferred R_t trajectories are practically indistinguishable across the two modeling specifications.

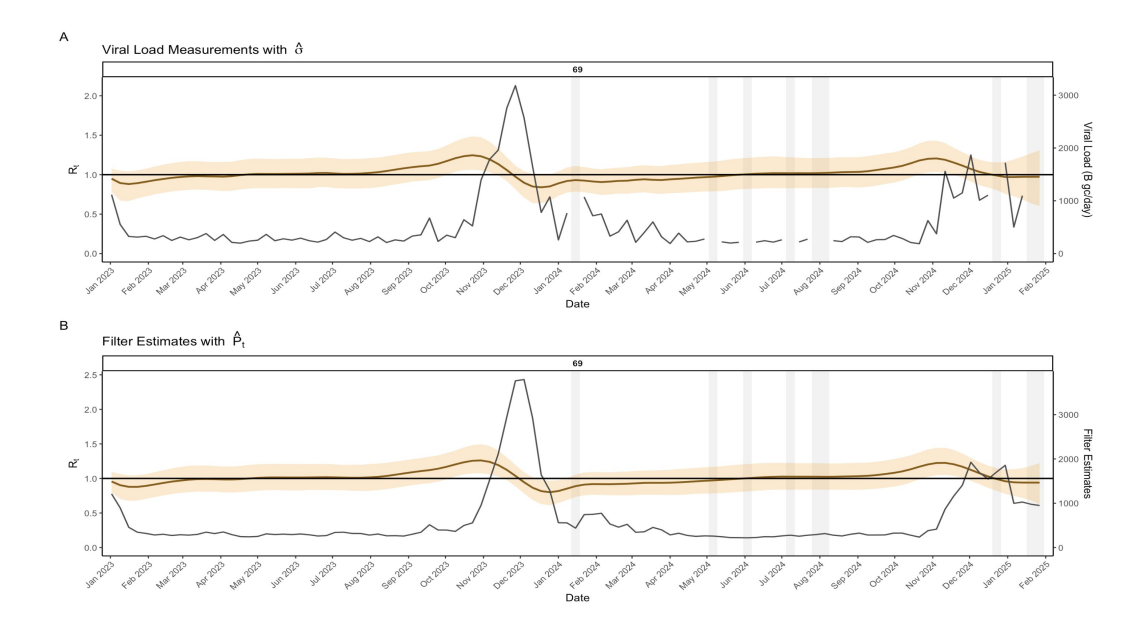


Figure 2: Effective reproduction number (R_t) with viral load on the right axis. Orange line: posterior mean of R_t ; orange band: 95% credible interval; horizontal line at $R_t = 1$; gray line: viral load (B gc/day). Panels A–B correspond, respectively, to: (A) BCPD with homoscedastic observation variance σ_y estimated; and (B) SSM-filtered trajectories with week-specific variances \hat{P}_t treated as known. Gray vertical bands represent periods with missing wastewater measurements.

To assess practical differences across specifications, Figure 3 contrasts weekly posterior means for R_t and I_t under (A) BCPD with homoscedastic noise and (B) SSM-filtered inputs with week-specific variances \hat{P}_t . For R_t , points fall close to the identity with minimal dispersion, indicating that estimates are largely insensitive to using filtered inputs with heteroscedastic variances. For I_t , dispersion is slightly larger—most visibly near peak weeks—but without a consistent bias. Overall, systematic differences are negligible and the inferred transmission trajectories are practically indistinguishable across the two specifications.

4 Discussion

We used a renewal framework with biologically motivated generation and shedding kernels to infer RSV transmission from wastewater. In contrast to more elaborate pipelines (e.g., EpiSewer) that couple multiple modules and assumptions, and ERN, which adds structural complexity to estimate R_t , our approach is intentionally parsimonious and transparent. Latent infections and observed load are linked through two kernels and a small set of identifiable parameters.

We evaluated two input/noise specifications that differ only in how the signal and its uncertainty enter the likelihood: (A) viral-load measurements in billions of copies per day (BCPD) with homoscedastic noise; and (B) SSM-filtered load estimates (FE) with week-specific Kalman variances \hat{P}_t treated as known. Convergence diagnostics were satisfactory in both cases (acceptable \hat{R} and low relative MCSE). Model comparison and pairwise scatter plots show that R_t is essentially invariant across A–B. For I_t , using

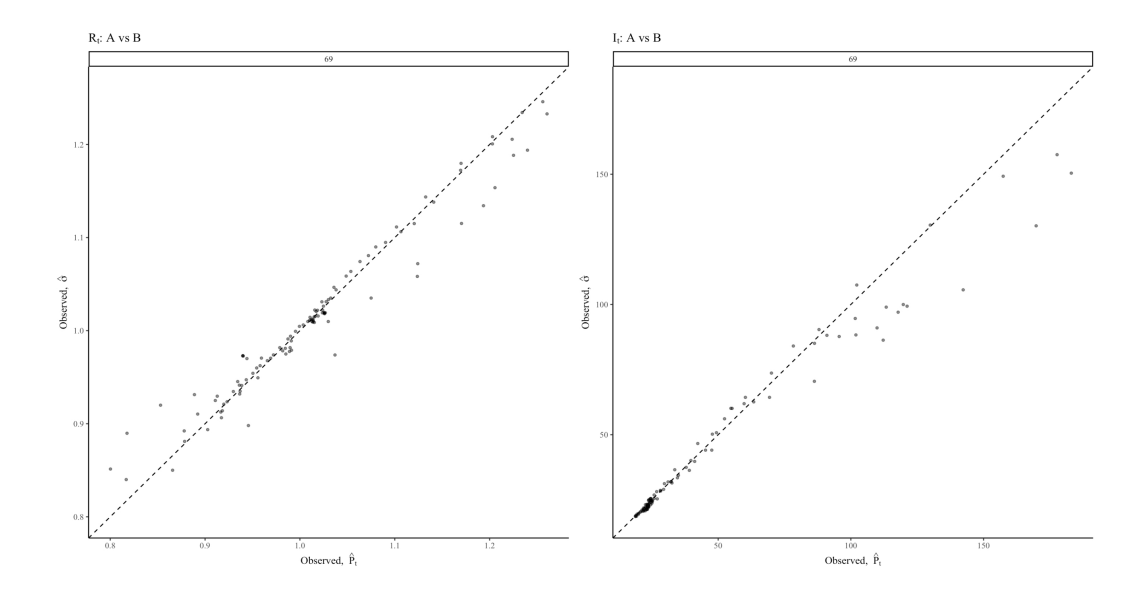


Figure 3: Comparison of weekly posterior means under specifications A (BCPD, homoscedastic σ_y) and B (SSM-filtered inputs with week-specific variances \hat{P}_t): left, R_t ; right, I_t . Points are weekly posterior means; the dashed line is the identity y = x.

FE with \widehat{P}_t (A vs. B) increases dispersion primarily in the upper tail; outside peak periods, trajectories are effectively equivalent. Given this pattern, the filtered input with \widehat{P}_t is attractive for routine reporting—because it carries week-specific observation variance—without altering the qualitative epidemiological interpretation.

Timing is consistent across the model specifications. The R_t maximum leads the wastewater maximum by about five weeks, and the I_t peak precedes the wastewater maximum by approximately one week. This ordering aligns with the generation and shedding kernels (on the order of 1–2 weeks) and the weekly aggregation of the series, supporting the renewal-based interpretation.

We also refit the model using concentration in copies per liter rather than flownormalized copies per day. Dimensionless parameters were essentially unchanged, whereas the plant-specific scale β shifted to absorb the unit change. Because switching units multiplies the observed signal by a constant, the model compensates by rescaling β while leaving shape and timing intact. In practice, the coefficients are scale-invariant except for β ; the inferred R_t trajectory is unaffected, and I_t changes only by a constant multiplicative factor tied to the measurement scale.

The absolute scale of I_t is not identified from wastewater alone, so we anchor it with $I_1 \sim \text{Poisson}(61)$, motivated by the fraction of Houston's population served by the selected sewershed and the city-wide mean weekly RSV cases. Sensitivity checks using alternative anchors for the initial condition confirm that peak timing and the ordering $R_t \to I_t \to \text{load}$ are preserved and that the R_t trajectory is robust; as expected, the level of I_t shifts nearly proportionally to the chosen anchor with compensating adjustments in β . Accordingly, we interpret I_t in relative terms.

5 Conclusions

Using a parsimonious renewal framework with generation and shedding kernels, we inferred RSV transmission from wastewater. We obtained the relative number of infections and the effective reproduction number with coherent timing: R_t leads I_t , and I_t leads the wastewater signal. Comparing two input choices—(A) measurements in billions of copies per day with homoscedastic noise; and (B) SSM-filtered load estimates with week-specific variances from the Kalman filter (\hat{P}_t) —we find R_t to be essentially invariant across specifications. For I_t , using filtered inputs with \hat{P}_t (A vs. B) increases dispersion primarily in the upper tail; outside peak periods, trajectories are effectively equivalent. Results are also robust to the measurement scale (gc/L vs. billions of copies per day): parameters are effectively unchanged except for the plant-specific scaling factor β , which absorbs unit changes. Overall, wastewater data coupled with a simple renewal structure provide stable estimates of I_t (in relative terms) and R_t without the need for complex preprocessing. When available, we therefore recommend using the SSM-filtered input as the default, with direct measurements retained as a robustness check.

Funding and Acknowledgments

The authors disclosed receipt of the following financial support for the research, authorship, and/or publication of this article: This work was supported by the Centers for Disease Control and Prevention (ELC-ED grant no. 6NU50CK000557-01-05 and ELC-CORE grant no. NU50CK000557). The authors acknowledge Houston Public Works for their contributions to the HHD WBE system. The authors would like to acknowledge the CDC National Wastewater Surveillance System (NWSS) scientific community. For more information on the Houston Wastewater Epidemiology Center of Excellence see https://www.hou-wastewater-epi.org.

Notes on contributor(s)

Palacio is the corresponding author, representing both intellectual leadership and implementation of the methodologies. He presented the team with a complete first draft for editorial comments. Ensor, Rice Co-PI of this project, led the technical development and draft writing. Keller consulted on developing the two-stage implementation with specific attention to uncertainty quantification. Schneider oversees the day-to-day implementation of the HHD WBE system and represents the team in national data analysis conversations. Domakonda serves as HHD manager for this project. Hopkins, serves as HHD PI for this project. Stadler, Rice Co-PI of this project, oversees all aspects of laboratory analyses, and brings the essential expertise in WBE. All authors contributed to the scientific discussion and edited the manuscript.

References

Johannes Bracher and Leonhard Held. Endemic-epidemic models with discrete-time serial interval distributions for infectious disease prediction. *International Journal of Forecasting*, 38(3):1221–1233, 2022. doi: 10.1016/j.ijforecast.2020.07.002.

- Muge Cevik, Pedro A. Piedra, Vittorio Demicheli, Cristina Cantarelli, Donatella Manno, Stefano Vergnano, Steve Pullan, and Rachel Harwood. Virology, transmission, and clinical features of respiratory syncytial virus in adults. *BMJ*, 380:e072292, 2023. doi: 10.1136/bmj-2022-072292.
- David Champredon, Irena Papst, and Warsame Yusuf. ern: An R package to estimate the effective reproduction number using clinical and wastewater surveillance data. *PLOS ONE*, 19(6):e0305550, 2024. doi: 10.1371/journal.pone.0305550.
- Perry de Valpine, Christopher Paciorek, Daniel Turek, Nick Michaud, Cliff Anderson-Bergman, Fritz Obermeyer, Claudia Wehrhahn Cortes, Abel Rodríguez, Duncan Temple Lang, Wei Zhang, Sally Paganin, Joshua Hug, Paul van Dam-Bates, Jagadish Babu, Lauren Ponisio, and Peter Sujan. nimble: MCMC, Particle Filtering, and Programmable Hierarchical Modeling, 2024. URL https://CRAN.R-project.org/package=nimble. R package version 1.3.0.
- John P. DeVincenzo, Chadi M. El Saleeby, and Andrew J. Bush. Respiratory syncytial virus load predicts disease severity in previously healthy infants. *Journal of Infectious Diseases*, 191(11):1861–1868, 2005. doi: 10.1086/430008.
- Katherine B. Ensor, Jacob C. Schedler, Jose Palacio, Rebecca Schneider, Karthik Domakonda, Loren Hopkins, and Lauren B. Stadler. A nonlinear hierarchical time series approach to citywide trend assessment of viruses, hot spot signals, and right-sizing system. *Data Science in Science*, 4(1), 2025. doi: 10.1080/26941899.2025.2559690. URL https://doi.org/10.1080/26941899.2025.2559690.
- Christophe Fraser. Estimating individual and household reproduction numbers in an emerging epidemic. *PLoS ONE*, 2(8):e758, 2007. doi: 10.1371/journal.pone.0000758.
- Laura Haak, Blaga Delic, Lin Li, Tatiana Guarin, Lauren Mazurowski, Niloufar Gharoon Dastjerdi, Aimee Dewan, and Krishna Pagilla. Spatial and temporal variability and data bias in wastewater surveillance of SARS-CoV-2 in a sewer system. *Science of The Total Environment*, 805:150390, 2022. doi: 10.1016/j.scitotenv.2021.150390.
- Caroline B. Hall, Caroline E. Long, and Katherine C. Schnabel. Respiratory syncytial virus infections in previously healthy working adults. *Clinical Infectious Diseases*, 33 (6):792–796, 2001. doi: 10.1086/322657.
- Oliver E. Hart and Rolf U. Halden. Computational analysis of SARS-CoV-2 surveillance by wastewater-based epidemiology locally and globally: Feasibility, economy, opportunities and challenges. *Science of The Total Environment*, 730:138875, 2020. doi: 10.1016/j.scitotenv.2020.138875.
- Xi He, Eric H. Y. Lau, Peng Wu, Xilong Deng, Jian Wang, Xinxin Hao, Yiu Chung Lau, Jessica Y. Wong, Yu Guan, Xinghua Tan, Xiaoneng Mo, Yanqing Chen, Baolin Liao, Weilie Chen, Fengyu Hu, Qing Zhang, Mingqiu Zhong, Yanli Wu, Zijian Zhao, Fuchun Zhang, Benjamin J. Cowling, Fang Li, and Gabriel M. Leung. Temporal dynamics in viral shedding and transmissibility of COVID-19. *Nature Medicine*, 26:672–675, 2020. doi: 10.1038/s41591-020-0869-5.

- Elizabeth E. Holmes, Eric J. Ward, and Kasper Wills. Marss: Multivariate autoregressive state-space models for analyzing time-series data. *The R Journal*, 4 (1):11-19, 2012. URL https://journal.r-project.org/archive/2012-1/RJournal_2012-1_Holmes~et~al.pdf.
- Houston Health Department. Respiratory diseases surveillance report: 2024-2025 influenza season, MMWR week 2025-02, 2025. URL https://www.houstonhealth.org/media/11526/download?inline=. Accessed 2025-09-30.
- Houston Public Works. City of houston wastewater operations report. https://www.publicworks.houstontx.gov/, 2023.
- Bridgette Hughes, Dorothea Duong, Bradley J. White, Krista R. Wigginton, Elana M. G. Chan, Marlene K. Wolfe, and Alexandria B. Boehm. Respiratory syncytial virus (RSV) RNA in wastewater settled solids reflects RSV clinical positivity rates. medRxiv preprint, 2021. URL https://doi.org/10.1101/2021.12.01.21267014. Posted December 5, 2021.
- Jana S. Huisman, Jérémie Scire, Lea Caduff, Xavier Fernandez-Cassi, Pravin Ganesanandamoorthy, Anina Kull, Andreas Scheidegger, Elyse Stachler, Alexandria B. Boehm, Bridgette Hughes, Alisha Knudson, Aaron Topol, Krista R. Wigginton, Marlene K. Wolfe, Tamar Kohn, Christoph Ort, Tanja Stadler, and Timothy R. Julian. Wastewater-based estimation of the effective reproductive number of SARS-CoV-2. *Environmental Health Perspectives*, 130(5):057011, 2022. doi: 10.1289/EHP10050.
- Adrian Lison, Hans-Michael Kaltenbach, Johannes S. Huisman, Tanja Stadler, Alessandra Rinaldo, Mathias Ackermann, and Niko Beerenwinkel. Estimating transmission dynamics from wastewater data using a bayesian generative modeling framework. *Nature Computational Science*, 3(6):540–548, 2023. doi: 10.1038/s43588-023-00466-6.
- David Lunn, Jessica Barrett, Michael Sweeting, and Simon Thompson. Fully bayesian hierarchical modelling in two stages, with application to meta-analysis. *Journal of the Royal Statistical Society: Series C (Applied Statistics)*, 62(4):551–572, 2013. doi: 10.1111/rssc.12007. URL https://doi.org/10.1111/rssc.12007.
- Mayo Clinic Staff. Respiratory syncytial virus (rsv)—symptoms & causes, 2023. URL https://www.mayoclinic.org/diseases-conditions/respiratory-syncytial-virus/symptoms-causes/syc-20353098. Accessed 2025-09-30.
- James Scott, Seth Flaxman, Swapnil Mishra, Samir Bhatt, H. Juliette T. Unwin, Axel Gandy, et al. epidemia: An r package for semi-mechanistic bayesian modeling of epidemics. arXiv, 2021. URL https://arxiv.org/pdf/2110.12461.
- Francesco Sera and Antonio Gasparrini. Extended two-stage designs for environmental research. *Environmental Health*, 21(41), 2022. doi: 10.1186/s12940-022-00853-z. URL https://doi.org/10.1186/s12940-022-00853-z.
- M. A. Vink, M. C. J. Bootsma, and J. Wallinga. Serial intervals of respiratory infectious diseases: A systematic review and analysis. *American Journal of Epidemiology*, 180 (9):865–875, 2014. doi: 10.1093/aje/kwu209.

Matthew J. Wade, Anna Lo Jacomo, Elena Armenise, Mathew R. Brown, Joshua T. Bunce, Graeme J. Cameron, Zhou Fang, Kata Farkas, Deidre F. Gilpin, David W. Graham, Jasmine M. S. Grimsley, Alwyn Hart, Till Hoffmann, Katherine J. Jackson, David L. Jones, Chris J. Lilley, John W. McGrath, Jennifer M. McKinley, Cormac McSparron, Behnam F. Nejad, Mario Morvan, Marcos Quintela-Baluja, Adrian M. I. Roberts, Andrew C. Singer, Célia Souque, Vanessa L. Speight, Chris Sweetapple, David Walker, Glenn Watts, Andrew Weightman, and Barbara Kasprzyk-Hordern. Understanding and managing uncertainty and variability for wastewater monitoring beyond the pandemic: Lessons learned from the united kingdom national COVID-19 surveillance programmes. Journal of Hazardous Materials, 424:127456, 2022. doi: 10.1016/j.jhazmat.2021.127456.

Appendix

1 Introduction

This appendix presents two scenarios that complement the main manuscript and use the same modeling specifications A–B: (A) BCPD with homoscedastic observation variance estimated; and (B) SSM-filtered trajectories with week-specific variances \hat{P}_t treated as known.

We re-fit the model using copies per liter (gc/L) instead of billions of copies per day (BCPD). This example isolates the role of units and flow normalization. As shown below, dimensionless parameters and inferred trajectories (R_t, I_t) are effectively unchanged, while the plant-specific scale β adjusts to absorb the unit change.

2 Analysis using gc/L

For R_t , the viral concentration panels in Fig. 4 sit essentially on top of their counterparts based on viral load: same autumn-2023 maximum, the dip around December–January, and the minor late-2024 rise. The concentration–load scatterplots in Fig. 6 reinforce this invariance—points hug the identity with correlations of 0.999 and very small MAE (0.002–0.003; Table 2). Parameter summaries are consistent with this picture: the dynamic/shape parameters (k, σ_{ϵ}) remain stable across A–B and across data types (Table 3). In short, R_t is unit-invariant: switching from viral load to viral concentration leaves the epidemiological signal unchanged.

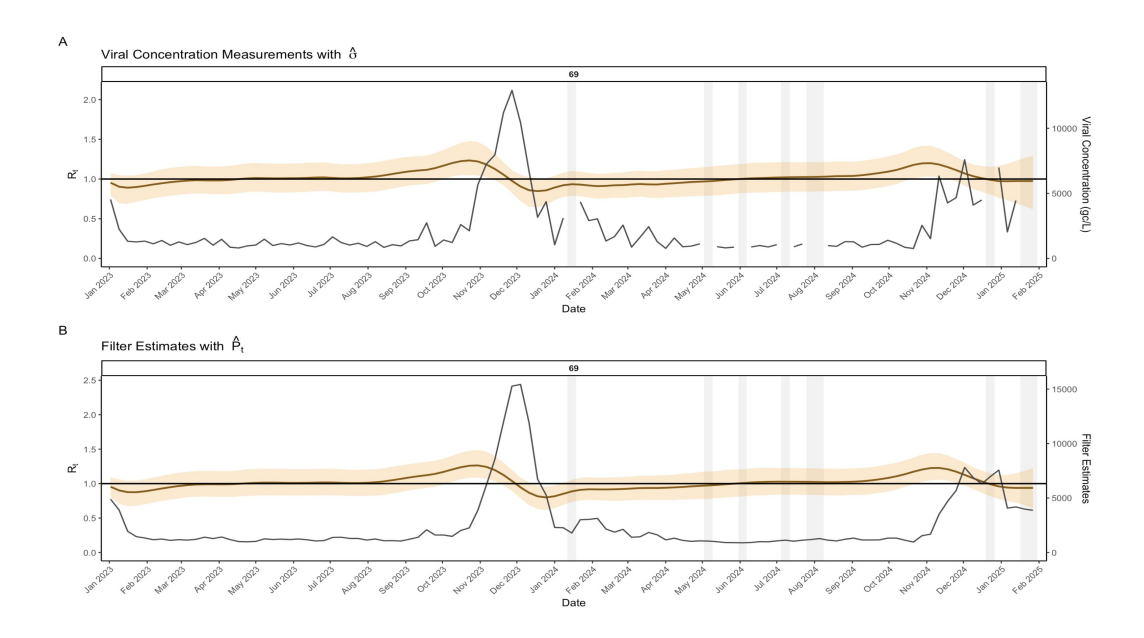


Figure 4: Effective reproduction number (R_t) with viral load on the right axis. Orange line: posterior mean of R_t ; orange band: 95% credible interval; horizontal line at $R_t = 1$; gray line: viral concentration (gc/L). Panels A–B correspond, respectively, to: (A) viral concentrations with homoscedastic observation variance σ_y estimated; and (B) SSM-filtered trajectories with week-specific variances \hat{P}_t treated as known.

For I_t , the viral concentration panels in Fig. 5 reproduce the same seasonality and peak timing as viral load (late-2023 peak, January decline, mild autumn-2024 uptick).

Concentration-based trajectories track load-based ones closely, with only small differences in magnitude during the peak and the late-2024 uptick. These differences are consistent with the modest MAE values for I_t (0.287–3.364 infections; Table 2) and reflect the expected β – I_t scale trade-off once flow is removed from the observation map. Timing is preserved and level shifts are minor, indicating that changes in data type affect units rather than the underlying epidemic pattern.

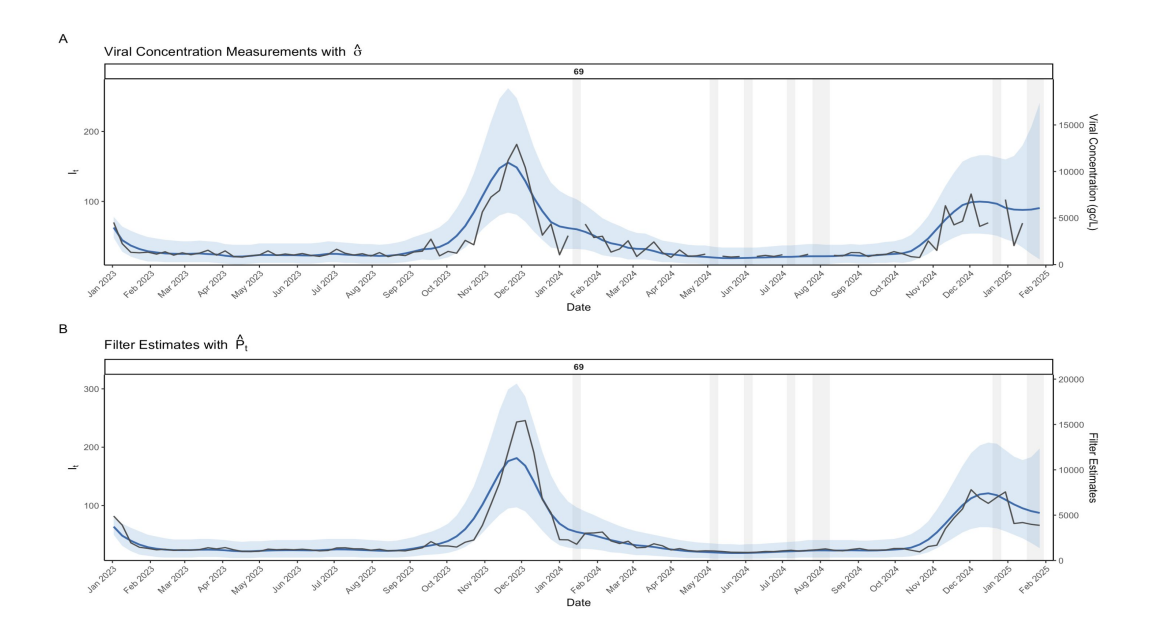


Figure 5: Latent incidence (I_t) with viral load on the right axis. Blue line: posterior mean of I_t ; blue band: 95% credible interval; gray line: viral concentration (gc/L). Panels A–B correspond, respectively, to: (A) viral concentrations with homoscedastic observation variance σ_y estimated; and (B) SSM-filtered trajectories with week-specific variances \hat{P}_t treated as known.

Metric	Model	Correlation	MAE
I_t	A	0.999	0.287
R_t	A	0.999	0.003
$\overline{I_t}$	В	0.999	3.364
R_t	В	0.999	0.002

Table 2: Agreement between viral concentration and viral load estimates (correlation and MAE) for I_t and R_t across models A–B.

Table 3 shows that k and σ_{ϵ} are empirically stable across data types. For example, the posterior means of k under load (A/B: 8.24/8.03) and under concentration (A/B: 8.48/8.02) are close, and their 95% credible intervals strongly overlap (e.g., model A k: [2.12, 18.68] in load vs. [2.37, 18.83] in concentration; model A σ_{ϵ} : [0.030, 0.135] vs. [0.025, 0.131]; similarly for model B with σ_{ϵ} : [0.032, 0.137] vs. [0.037, 0.132]). Mean shifts are small relative to posterior spreads, supporting the view that these parameters are invariant to the data type. By design, β changes scale and absorbs unit effects.

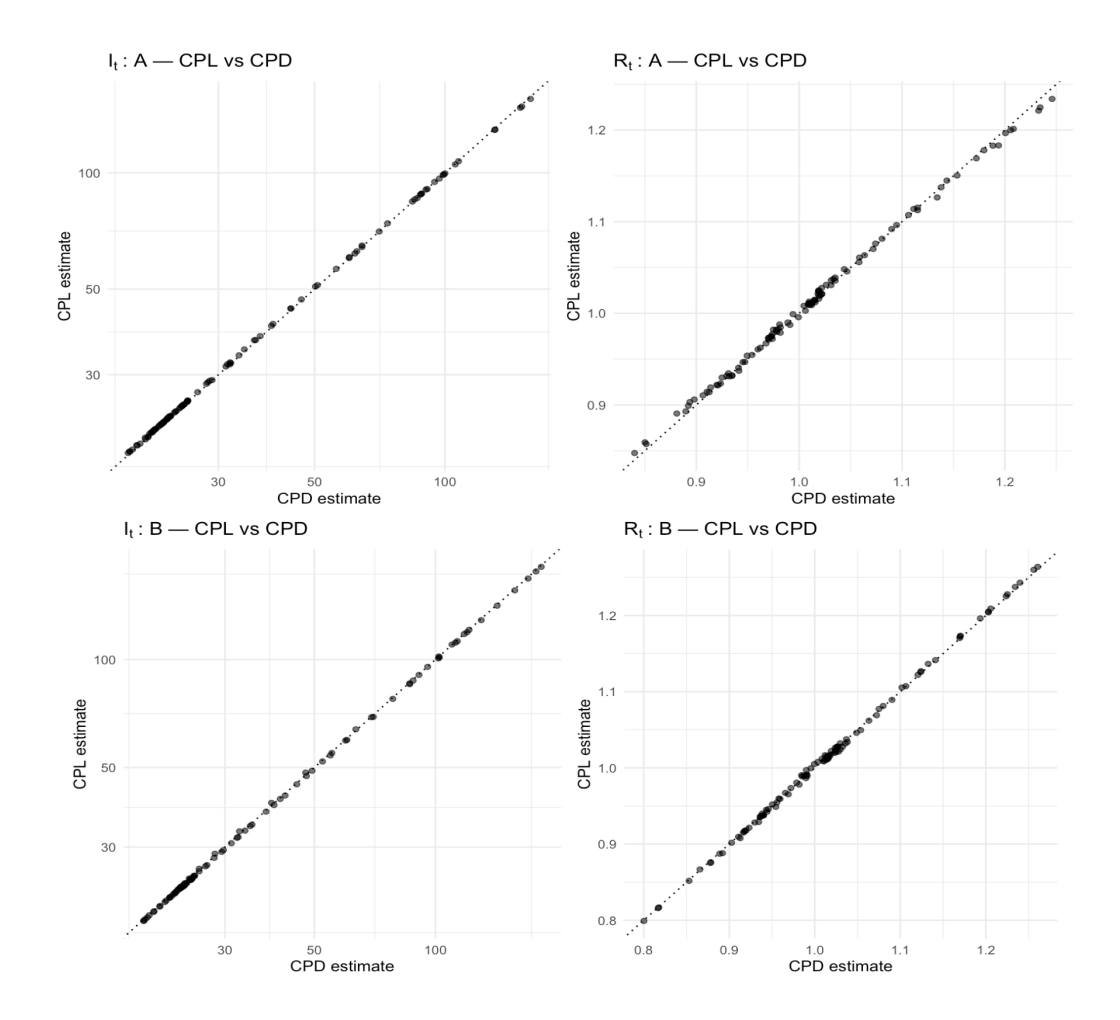


Figure 6: Pairwise scatterplots comparing estimates from viral concentration (CPL) and viral load (CPD) for I_t (left) and R_t (right) under models A–B. Points are weekly posterior means; the dashed line is y=x.

For the observational noise σ_y , posteriors are also close across data types (e.g., $\sigma_{y,\text{load}} = 0.385 \, [0.316, 0.466] \, \text{vs.}$ $\sigma_{y,\text{conc}} = 0.387 \, [0.319, 0.466]$).

Parameter	Model	Mean	St.Dev.	95% CI
k	A	8.483	4.685	[2.367, 18.829]
σ_ϵ	A	0.069	0.027	[0.025, 0.131]
β	A	54.847	12.572	$[34.224,\ 82.537]$
σ_y	A	0.387	0.037	[0.319, 0.466]
k	В	8.018	4.680	[1.974, 18.596]
σ_ϵ	В	0.079	0.024	[0.037, 0.132]
β	В	59.988	15.416	[36.055, 96.459]

Table 3: Posterior summaries for models A–B using viral concentration (gc/L).